AIMS Mathematics, 11(1): 1998–2026.
DOI: 10.3934/math.2026083
Received: 20 November 2025
Revised: 10 January 2026
Accepted: 15 January 2026
Published: 21 January 2026

http://www.aimspress.com/journal/Math

Research article

New solitons and bifurcation dynamics in the fractional Huxley model: Numerical and analytical approaches

Huiqin Chu[1], Muhammad Abuzar[2], Mohammed Ahmed Alomair[3,*] and Abdulaziz Khalid Alsharidi[4]

[1] School of Mathematics-Physics and Finance, Anhui Polytechnic University, Wuhu, Anhui, 241000, China
[2] School of Mathematical Sciences, Guizhou Normal University, Guiyang, Yunyan 550003, China
[3] Department of Quantitative Methods, School of Business, King Faisal University, Al-Ahsa 31982, Saudi Arabia
[4] Department of Mathematics and Statistics, College of Science, King Faisal University, Al-Ahsa 31982, Saudi Arabia

* **Correspondence:** Email: ma.alomair@kfu.edu.sa.

Abstract: This research explores the higher-order nonlinear fractional Huxley equation formulated with the β, and M-truncated fractional derivatives to account for memory and hereditary effects present in nonlinear diffusion and excitation wave dynamics. The fractional formulation expands on the standard Huxley model by incorporating nonlocal temporal and spatial correlations, providing a more realistic description of finite-amplitude wave propagation and spectral energy transfer in complex media. Two advanced analytical techniques are used to derive exact solutions: the enhanced modified extended tanh expansion method (EMETEM) and the improved F-expansion technique. Compared to classic perturbation and variational techniques, these methods offer greater algebraic freedom and faster convergence, resulting in a diverse family of closed-form traveling-wave solutions expressed in trigonometric, hyperbolic, exponential, and rational forms. The analytical results are further validated, and the spatiotemporal evolution of the resulting wave structures is investigated using a finite-difference numerical scheme. The accuracy and robustness of the suggested framework are confirmed by the numerical findings, which show good agreement with the analytical results. Phase-plane and bifurcation analyses demonstrate transitions between periodic, quasi-periodic, and chaotic regimes by revealing both stable and unstable spiral formations. The findings show that fractional derivatives significantly improve the dynamical characteristics of the Huxley system by allowing for finer control of diffusion, dispersion, and localized energy concentration, advancing our understanding of nonlinear fractional wave behavior in excitable and dispersive media.

Keywords: fractional Huxley model; computational approaches; exact solutions; finite-difference

scheme; phase portraits and bifurcation analysis
Mathematics Subject Classification: 35C08, 35Q55, 37K40

1. Introduction

Fractional differential equations (FDEs), which are differential equations containing non-integer orders of differentiation, have become an effective tool for simulating complicated dynamical systems with memory, spatial heterogeneity, and nonlocal interactions. Fractional models, in contrast to traditional integer-order formulations, provide a more accurate depiction of diffusion, dispersion, and relaxation processes by including the process's history into the governing dynamics. FDEs have been widely used in many different fields of science and engineering over the past few decades, such as nonlinear wave propagation [1, 2], viscoelastic and rheological systems [3, 4], heat and mass transfer [5], control and signal processing [6], and plasma or optical physics [7]. They are an essential part of the study of complicated physical processes because of their capacity to combine diffusion-like and wave-like characteristics into a single framework. Particularly, anomalous transport, subdiffusion, and energy localization phenomena that are beyond the scope of conventional differential models have been successfully described by fractional operators. As a result, investigating analytical and numerical techniques to solve fractional equations has emerged as a crucial area in contemporary theoretical physics and applied mathematics [8, 9].

Researchers have concentrated on examining stability, finding precise solutions, and creating effective numerical techniques since the existence and uniqueness results for fractional systems were established [10–12]. In many scientific domains, such as fluid mechanics, plasma dynamics, diffusion processes, and fractal systems, fractional partial differential equations (FPDEs) are crucial for modeling and simulation. Numerous mathematical methods have been devised to find analytical and semi-analytical solutions of FPDEs. Examples include the new auxiliary equation method [13], the variational iteration method [14], the exp-function approach [15], the first integral technique [16], the $\exp(-\phi(\xi))$ expansion method [17], and many more [18, 19].

Nonlinear effects play a central role in wave propagation through dispersive and dissipative media, and Huxley-type equations are widely used to describe limited-amplitude waves and nonlinear reaction-diffusion processes with strong mode interactions [13, 20–22]. Owing to their ability to capture oscillatory and excitable dynamics, the Huxley model and its fractional extensions have found applications in ocean engineering, plasma physics, nonlinear optics, and biological signal transmission [23, 24]. In particular, the fractional-order formulation incorporates memory and hereditary effects absent from the classical integer-order model whereas reducing to the standard Huxley equation as the fractional order approaches unity. Recent studies have reported exact solitary-wave solutions via analytical schemes, developed efficient numerical methods for fractional Burger-Huxley-type models, and proposed data-driven solvers such as fractional physics-informed neural networks for one- and two-dimensional settings [22]. These developments motivate the present work, which introduces a unified analytical-numerical framework combined with bifurcation-based dynamical analysis to extend existing results for the governing fractional Huxley equation.

In recent years, several analytical approaches have been developed to derive closed-form or

approximate solutions of nonlinear fractional differential equations, including the integral transform method [25], modified trial equation approach [26], subequation method [27], and Kudryashov scheme [28–30]. While these techniques have enhanced the understanding of fractional systems, their convergence and adaptability often remain restricted by the complexity of fractional operators and nonlinear terms. Earlier work on the fractional Huxley equation, such as the study reported in [13], applied the new auxiliary equation method to obtain soliton solutions and examine modulation instability. However, that study did not explore the bifurcation structure, stability, or numerical realization of the fractional model, leaving these aspects insufficiently addressed [31–33].

To close this gap, the current study adds the β and M-truncated fractional derivatives [34, 35], which effectively incorporate nonlocal and memory-dependent effects, to the theoretical and computational framework of the Huxley fractional equation. Some fractional operators yield sharper localization of wave structures, capturing more pronounced peaks and troughs compared to the classical model. Other operators, on the other hand, improve stability and smoothness whereas lowering oscillations and numerical artifacts in the solution. Thus, the choice of fractional operator allows control over both the localization and stability of the system, highlighting the flexibility and richness introduced by fractional-order formulations. Different traveling-wave solutions in trigonometric, hyperbolic, exponential, and rational forms are constructed using two complementary analytical methods: the enhanced modified extended tanh expansion method (EMETEM) [36, 37] and improved F-expansion method [38, 39]. Compared to earlier well-established techniques, these formulations provide more flexibility and expand the current analytical environment. The analytical solutions, numerical simulations, and bifurcation analysis reported in this work show deeper insights into dynamical characteristics of the fractional model, such as modified wave propagation, stability features, and bifurcation structures.

A finite-difference numerical approach [40] is used to simulate the spatiotemporal evolution of the fractional wave profiles in order to guarantee the dependability and physical consistency of the results produced. The robustness of resulting solutions is confirmed by the numerical results, which exhibit excellent agreement with the analytical predictions. Comparing these schemes allows us to observe how numerical discretization can influence the qualitative behavior of solutions. For consistency, all methods use the same set of parameter values, ensuring that any differences are solely due to the numerical methodology. Furthermore, a thorough bifurcation analysis [41, 42] is carried out to investigate how changes in system characteristics affect dynamical transitions and stability.

A range of analytical and numerical methods have been developed recently to investigate nonlinear fractional differential equations, such as the traditional Huxley equation, that arise in biological and physical models. Traditional analytical approaches such as the Adomian decomposition, variational iteration, homotopy perturbation, and standard tanh-function methods have been widely employed due to their simplicity. However, these approaches frequently fail to represent the rich dynamical behavior of fractional-order systems, rely on restricted assumptions, or offer solutions in constrained convergence areas. In contrast, the extended modified expanded tanh-expansion method adopted in this study offers greater flexibility in constructing exact and approximate analytical solutions by incorporating a broader functional structure, enabling the capture of diverse wave patterns and nonlinear interactions more effectively. Although spectral and finite element approaches are known for their great accuracy, their implementation for fractional operators can be difficult and computationally taxing. The finite difference scheme employed here provides a balance between

computational efficiency and accuracy, making it suitable for long-time simulations. Additionally, a deeper comprehension of the qualitative dynamics of the fractional Huxley model, which is sometimes disregarded in solely numerical or analytical studies, is made possible by the inclusion of bifurcation analysis.

This framework improves both the accuracy and interpretability of solutions compared to classical methods. The EMETEM offers several advantages over classical techniques, including the ability to systematically construct exact and approximate analytical solutions and to capture a wide range of nonlinear wave structures. However, its applicability is mainly limited to nonlinear equations where the balancing procedure can be performed, and it may become cumbersome for highly complicated or higher-dimensional systems. Compared to traditional techniques such as the Exp-function method or auxiliary equation methods, the EMETEM and F-expansion method provide greater flexibility in constructing exact and approximate solutions. These methods can capture more diverse wave structures, handle higher-order nonlinearities effectively, and offer a systematic framework for obtaining analytical solutions, which is often challenging for classical approaches. In order to generate precise numerical solutions that are utilized to verify the analytical conclusions through quantitative comparisons, we employ a finite difference scheme. Then, bifurcation analysis is used to explore the qualitative dynamics and stability properties of the fractional model, providing insights that are not available from purely analytical or numerical studies alone. Finally, we highlight the importance of the fractional-order formulation, which captures memory and hereditary effects, leading to richer dynamical behavior compared to the classical integer-order model.

The remainder of this paper is organized as follows. Section 2 provides essential definitions and properties of fractional calculus. Section 3 presents the governing form of the fractional Huxley equation. Section 4 details the employed analytical methods, including both the F-expansion and EMETEM formulations. Section 5 discusses the construction of exact analytical solutions, whereas Section 6 illustrates their dynamic characteristics through graphical interpretation. Section 7 explains the numerical implementation and the comparison between analytical and numerical results. Section 8 focuses on the qualitative bifurcation analysis, and Section 9 concludes the study with major findings and possible directions for future research.

2. Basic results of fractional calculus

Giving some basic definitions of fractional calculus is the sole objective of this section.

2.1. β-derivative conceptions

The fractional β-derivative is defined as follows [34]:

$$ {}_{0}^{A}\mathcal{D}_{z}^{\delta}(\mathcal{M}_1(z)) = \lim_{r\to 0} \frac{\mathcal{M}_1\left(z + r(z+\frac{1}{\Gamma(\delta)})^{1-\delta}\right) - \mathcal{M}_1(z)}{r}, \quad 0 < \delta < 1. \tag{2.1} $$

It possesses the following qualities:

1: ${}_{0}^{A}\mathcal{D}_{z}^{\delta}(a\ \mathcal{M}_1(z) + b\ \mathcal{M}_2(z)) = a\,{}_{0}^{A}\mathcal{D}_{z}^{\delta}\mathcal{M}_1(z) + b\,{}_{0}^{A}\mathcal{D}_{z}^{\delta}\mathcal{M}_2(z)$,

2: $\mathcal{D}_{z}^{\delta}(c) = 0$,

3: ${}_0^A\mathcal{D}_z^\delta(\mathcal{M}_1(z) * \mathcal{M}_2(z)) = \mathcal{M}_2(z){}_0^A\mathcal{D}_z^\delta\mathcal{M}_1(z) + \mathcal{M}_1(z){}_0^A\mathcal{D}_z^\delta\mathcal{M}_2(z),$

4: ${}_0^A\mathcal{D}_z^\delta\left(\frac{\mathcal{M}_1(z)}{\mathcal{M}_2(z)}\right) = \frac{\mathcal{M}_2(z){}_0^A\mathcal{D}_z^\delta\mathcal{M}_1(z) - \mathcal{M}_1(z){}_0^A\mathcal{D}_z^\delta\mathcal{M}_2(z)}{\mathcal{M}_2^2(z)}.$

The β-fractional integral is defined as follows [43]:

$$ {}_0^AI_t^\delta\mathcal{M}_1(z) = \int_0^z \left(\psi + \frac{1}{\Gamma(\delta)}\right)^{1-\delta}\mathcal{M}_1(\zeta)d\zeta. \tag{2.2}$$

Theorem 1. *Let $\gamma = [\mathrm{Re}(\nu)] + 1$ for $\mathrm{Re}(\nu) \geq 0$. Let $\mathcal{M} \in C_{\delta,l}^{\gamma}([l,m])$ be a function. For example, $\mathcal{M} \in C_{\delta,m}^{\gamma}([l,m])$. Next, the left- and right β-type conformable derivatives' Riemann–Liouville formulations are provided as follows:*

$$\begin{aligned} {}_l^{AR}{}^{\nu}\mathcal{D}_z^\delta\mathcal{M}_1(z) &= \frac{{}_l^A{}^{\gamma}\mathcal{D}_z^\delta}{\Gamma(\gamma-\nu)}\int_{\frac{-l}{\Gamma(\delta)}}^{z}\left[\frac{(z+\frac{l}{\Gamma(\delta)})^\delta - (x+\frac{l}{\Gamma(\delta)})^\delta}{\delta}\right]^{\gamma-\nu-1} \\ &\times\frac{\mathcal{M}_1(x)}{(x+\frac{1}{\Gamma(\delta)})^{1-\delta}}dx \\ &={}_l^A{}^{\gamma}\mathcal{D}_l^\delta({}_l^A{}^{\gamma-\nu}I_l^\delta\mathcal{M}_1(z)) \end{aligned} \tag{2.3}$$

and

$$\begin{aligned} {}_z^{AR}{}^{\nu}\mathcal{D}_m^\delta\mathcal{M}_1(z) &= \frac{(-1)^\gamma{}_\gamma^A{}^z\mathcal{D}_m^\delta}{\Gamma(\gamma-\nu)}\int_z^{\frac{-m}{\Gamma(\delta)}}\left[\frac{(z+\frac{m}{\Gamma(\delta)})^\delta - (x+\frac{m}{\Gamma(\delta)})^\delta}{\delta}\right]^{\gamma-\nu-1} \\ &\times\frac{\mathcal{M}_1(x)}{(x+\frac{m}{\gamma(\delta)})^{1-\delta}}dx \\ &={}_z^A{}^{\gamma}\mathcal{D}_m^\delta({}_z^A{}^{\gamma-\nu}I_m^\delta\mathcal{M}_1(z)). \end{aligned} \tag{2.4}$$

2.2. M-truncated fractional derivative

Definition 1. *The Mittag-Leffler function with a single parameter is described as [35]:*

$$ {}_iE_\delta(\mathcal{M}) = \sum_{n=0}^{i}\frac{\mathcal{M}^n}{\Gamma(\delta n+1)}, \tag{2.5}$$

in which $\delta > 0$ and $n \in C$. It is defined in terms of a non-fuzzy idea as follows:

Definition 2. *Let $\mathcal{M}_1 : [0,\infty) \to \mathbb{R}$ and $0 < \delta < 1$. The following represents the M-truncated derivative of $\mathcal{M}_1$ of order δ:*

$$ {}_i\mathcal{D}_M^{\delta,\chi}\mathcal{M}_1(z) = \lim_{\varepsilon\to 0}\frac{\mathcal{M}_1(z+{}_iE_\chi(\varepsilon z^{-\delta})) - \mathcal{M}_1(z)}{\varepsilon}, \tag{2.6}$$

$\forall\ z > 0$ and ${}_iE_\chi(.)$, $\chi > 0$.

Theorem 2. *Given $\delta \in (0,1]$ and $\chi > 0$, and assuming that $\mathcal{M}_1$ is a differentiable function of δ order at $z_0 > 0$, $\mathcal{M}_1$ is continuous at z_0.*

Theorem 3. *Suppose that $\delta \in (0, 1]$, $\chi > 0$, $\kappa, \lambda \in \mathbb{R}$ and $\mathcal{M}_1$, $\mathcal{M}_2$ are δ-differentiable at $z > 0$, then*

1) ${}_i\mathcal{D}_M^{\delta,\chi}(\kappa\mathcal{M}_1(z) + \lambda\,\mathcal{M}_2(z)) = \kappa\mathcal{D}_M^{\delta,\chi}(\mathcal{M}_1(z)) + \lambda\mathcal{D}_M^{\delta,\chi}(\mathcal{M}_2(z))$.

2) ${}_i\mathcal{D}_M^{\delta,\chi}(\mathcal{M}_1(z) * \mathcal{M}_2(z)) = \mathcal{M}_1(z) * \mathcal{D}_M^{\delta,\chi}(\mathcal{M}_2(z)) + \mathcal{M}_2(z) * \mathcal{D}_M^{\delta,\chi}(\mathcal{M}_1(z))$.

3) ${}_i\mathcal{D}_M^{\delta,\chi}(\frac{\mathcal{M}_1(z)}{\mathcal{M}_2(z)}) = \frac{\mathcal{M}_1(z)\mathcal{D}_M^{\delta,\chi}(\mathcal{M}_2(z)) - \mathcal{M}_2(z)\mathcal{D}_M^{\delta,\chi}(\mathcal{M}_1(z))}{[\mathcal{M}_2(z)]^2}$.

4) ${}_i\mathcal{D}_M^{\delta,\chi}(\phi) = 0$, *where $\mathcal{M}_1 = \phi$ is a constant.*

5) *When $\mathcal{M}_1(z)$ is differentiable,* ${}_i\mathcal{D}_M^{\delta,\chi}(\mathcal{M}_1)(z) = \frac{z^{1-\delta}}{\Gamma(\chi+1)}\frac{d\mathcal{M}_1(z)}{dz}$.

The remaining parameters and symbols appearing throughout the manuscript are summarized in Table 1 for clarity.

Table 1. Notation used in the manuscript.

Symbol	Description	Notes
$P(x,t)$	Dependent variable (solution function)	—
x	Spatial variable	$x \in \mathbb{R}$
t	Time variable	$t > 0$
δ	Order of the fractional derivative	$0 < \alpha \leq 1$
σ	real constants	model-dependent
$\mathcal{D}_{M,t}^{\delta,\rho}$, $\mathcal{D}_t^{\delta}$	Fractional derivative operators	see Eq (3.1)
$\Gamma(\cdot)$	Gamma function	standard definition
$U(\eta)$	Traveling-wave profile	$P(x,t) = U(\eta)$
η	Traveling-wave coordinate	See Eqs (3.4) and (3.5)
k	Wave number / scaling constant	$k \neq 0$
ψ	Wave speed	Eq (3.4)
Δx	Spatial step size	numerical method
Δt	Time step size	numerical method
P_i^n	Numerical approximation of $P(x,t)$	at (x_i, t_n)

3. Fractional governing model

The Huxley equation [21] in its time-fractional form is written as

$$\begin{cases} \mathcal{D}_{M,t}^{\delta,\rho}P(x,t) - \mathcal{D}_{M,x}^{2\delta,\rho}P(x,t) = \sigma\,P(x,t)[\,\alpha(1-P(x,t))P(x,t) - \theta], \\ \mathcal{D}_t^{\delta}P(x,t) - \mathcal{D}_x^{2\delta}P(x,t) = \sigma\,P(x,t)[\,\alpha(1-P(x,t))P(x,t) - \theta\,], \qquad 0 < \delta \leq 1, \end{cases} \tag{3.1}$$

where δ is the fractional order of the time derivative, and σ is a nonzero real constant. Eq (3.1) can be transformed by expanding the nonlinear term on the right-hand side. Equation (3.1) represents the fractional Huxley model under two nonlocal derivative formulations: the M-truncated fractional derivative $\mathcal{D}_{M,t}^{\delta,\rho}$ and the classical β-fractional derivative $\mathcal{D}_t^{\delta}$. This model generalizes the classical Huxley equation by incorporating memory effects through fractional-order dynamics, allowing for more accurate descriptions of wave propagation and excitable media. The present work systematically investigates both nonlocal operators, deriving a diverse set of analytical solutions, including soliton,

trigonometric, and Jacobi elliptic waveforms, whereas simultaneously validating the results via numerical simulations. This dual-operator framework enables a direct comparison of memory truncation effects and provides new insights into the influence of fractional dynamics on the amplitude, width, and stability of wave propagation in excitable biological systems.

$$\begin{cases} \mathcal{D}_{M,t}^{\delta,\rho} P(x,t) - \mathcal{D}_{M,x}^{2\delta,\rho} P(x,t) + \sigma P^3(x,t) - \sigma(1+\theta)P^2(x,t) + \sigma\theta P(x,t) = 0, \\ \mathcal{D}_t^{\delta} P(x,t) - \mathcal{D}_x^{2\delta} P(x,t) + \sigma P^3(x,t) - \sigma(1+\theta)P^2(x,t) + \sigma\theta P(x,t) = 0, \qquad 0 < \delta \leq 1. \end{cases} \tag{3.2}$$

To construct traveling-wave solutions, the dependent variable $P(x,t)$ is assumed in the form

$$P(x,t) = U(\eta), \tag{3.3}$$

where $U(\eta)$ is a single-variable function of the traveling coordinate η, and $P(x,t)$ is the soliton-like pulse profile. The traveling coordinate for the β-fractional operator is defined as

$$\eta = kx - \frac{\psi}{\delta} t^{\delta} \left(1 + \frac{1}{\Gamma(\delta)}\right)^{\delta}, \tag{3.4}$$

where k denotes the wave number, ψ is the wave velocity, and $\Gamma(\cdot)$ represents the gamma function.

In the case of the M-truncated fractional operator, the corresponding transformation is taken as

$$\eta = kx - \frac{\Gamma(\rho+1)}{\delta} \psi\, t^{\delta}, \tag{3.5}$$

with ρ being a positive real parameter associated with the truncation index.

Substituting either of the transformations (3.4) or (3.5) into Eq (3.2) reduces the fractional partial differential equation to a nonlinear ordinary differential equation of the form

$$-\psi\, U'(\eta) - k^2 U''(\eta) + \sigma U^3(\eta) - \sigma(1+\theta)U^2(\eta) + \sigma\theta U(\eta) = 0, \tag{3.6}$$

where the first and second derivatives of U with respect to η are denoted by $U'(\eta)$ and $U''(\eta)$. Thus, the simplified governing model that characterizes the propagation of fractional traveling waves within the Huxley framework is represented by Eq (3.6), which serves as the foundation for additional analytical and numerical investigation.

4. Analytical solution approaches

In this study, two dependable analytical frameworks are used to get exact solutions to the nonlinear evolution equations under consideration. The first method is the EMETEM, which has been shown to be an effective and methodical way to build soliton-like and other closed-form solutions. This approach reduces the controlling fractional equation to a solvable ordinary differential form by using appropriate variable transformations and function expansions. The subsequent approach used is the classical F-expansion method, which makes it easier to create both periodic and solitary wave profiles by representing the solutions using trigonometric and hyperbolic functions. This section aims to present a wider class of analytical solutions for the fractional Huxley model under consideration and to assess and compare the performance of EMETEM and the F-expansion approach.

For nonlinear fractional differential equations, the EMETEM offers a methodical, analytical approach that produces precise and flexible solutions. It captures a broader spectrum of nonlinear dynamic behaviors and improves the precision of found solutions by using extended hyperbolic function expansions.

Consider a general nonlinear partial differential equation of the form

$$P(U, U_x, U_t, U_{xx}, U_{xt}, U_{tt}, \ldots) = 0, \tag{4.1}$$

where $U(x,t)$ denotes the dependent variable. To transform Eq (4.1) into an ordinary differential equation, we introduce the traveling-wave variable:

$$U(x,t) = U(\eta).$$

Substituting this transformation into Eq (4.1) leads to

$$U(\zeta, \zeta', \zeta'', \zeta^{(m)}, \ldots) = 0, \quad \zeta = \zeta(\eta), \tag{4.2}$$

where primes indicate derivatives with respect to ζ.

The assumed solution form for EMETEM is expressed as

$$U(\eta) = M_0 + \sum_{i=1}^{m} M_i[\zeta(\eta)]^i + \sum_{i=1}^{m} N_i[\zeta(\eta)]^{-i}, \tag{4.3}$$

where M_0, M_1, …, M_i, N_1, N_2, …, N_i are constants to be determined. The function $\zeta(\eta)$ satisfies the Riccati equation

$$\frac{d\zeta}{d\eta} = J + \zeta^2, \tag{4.4}$$

where J is a real-valued parameter.

Substituting Eqs (4.3) and (4.4) into Eq (4.2) and then equating coefficients of identical powers of $\eta(\zeta)$ yields a system of algebraic equations involving the unknown constants

$$J, M_0, M_1, M_2, \ldots, M_m, M_{-1}, M_{-2}, \ldots, M_{-m}, N_1, N_2.$$

By setting each coefficient to zero, these constants are determined explicitly. The general solutions of Eq (4.4) depend on the sign of J, leading to multiple categories of wave structures as follows.

For $J < 0$ (hyperbolic-type solutions):

$$\begin{aligned}
\zeta_1(\eta) &= -\sqrt{-J}\tanh(\sqrt{-J}\eta), \\
\zeta_2(\eta) &= -\sqrt{-J}\coth(\sqrt{-J}\eta), \\
\zeta_3(\eta) &= -\sqrt{-J}[\tanh(2\sqrt{-J}\eta) + i\omega\,\mathrm{sech}(2\sqrt{-J}\eta)], \\
\zeta_4(\eta) &= \frac{J - \sqrt{-J}\tanh(\sqrt{-J}\eta)}{1 + \sqrt{-J}\tanh(\sqrt{-J}\eta)}, \\
\zeta_5(\eta) &= \frac{\sqrt{-J}[5 - 4\cosh(2\sqrt{-J}\eta)]}{3 + 4\sinh(2\sqrt{-J}\eta)},
\end{aligned}$$

$$\zeta_6(\eta) = \frac{\omega\sqrt{-J(m^2+n^2)} - m\sqrt{-J}\cosh(2\sqrt{-J}\eta)}{m\sinh(2\sqrt{-J}\eta) + n},$$
$$\zeta_7(\eta) = \omega\sqrt{-J}\left(1 - \frac{2m}{m + \cosh(2\sqrt{-J}\eta) - \omega\sinh(2\sqrt{-J}\eta)}\right).$$

For $J > 0$ (trigonometric-type solutions):

$$\zeta_8(\eta) = \sqrt{J}\tan(\sqrt{J}\eta),$$
$$\zeta_9(\eta) = -\sqrt{J}\cot(\sqrt{J}\eta),$$
$$\zeta_{10}(\eta) = \sqrt{J}[\tan(2\sqrt{J}\eta) + \omega\sec(2\sqrt{J}\eta)],$$
$$\zeta_{11}(\eta) = -\sqrt{J}\left(\frac{1 - \tan(\sqrt{J}\eta)}{1 + \tan(\sqrt{J}\eta)}\right),$$
$$\zeta_{12}(\eta) = -\sqrt{J}\left(\frac{4 - 5\cos(2\sqrt{J}\eta)}{3 + 5\sin(2\sqrt{J}\eta)}\right),$$
$$\zeta_{13}(\eta) = \frac{\omega\sqrt{J(m^2-n^2)} - m\sqrt{J}\cos(2\sqrt{J}\eta)}{m\sin(2\sqrt{J}\eta) + n},$$
$$\zeta_{14}(\eta) = i\omega\sqrt{J}\left(1 - \frac{2m}{m + \cos(2\sqrt{J}\eta) - i\omega\sin(2\sqrt{J}\eta)}\right).$$

For $J = 0$ (rational solutions):

$$\zeta_{15}(\eta) = -\frac{1}{\eta}. \tag{4.5}$$

These solutions, which correspond to various physical regimes and parameter conditions, represent a broad variety of nonlinear structures, including rational forms, periodic solutions, and solitary waves. Thus, a thorough analytical framework for studying the fractional Huxley equation and associated nonlinear systems is provided by the combined use of EMETEM and the F-expansion techniques.

4.1. F-expansion method

To construct explicit wave solutions of the nonlinear partial differential equations, we employ the F-expansion procedure, which has been proven effective for generating a variety of solitary and periodic wave profiles. Consider the general nonlinear partial differential equation

$$P(U, U_x, U_t, U_{xt}, U_{xx}, \dots) = 0, \tag{4.6}$$

where P denotes a polynomial operator acting on the dependent variable $U(x,t)$ and its derivatives with respect to the spatial variable x and temporal variable t.

To reduce the above equation to an ordinary differential form, we introduce a traveling-wave transformation as follows:

$$P(x,t) = \Omega(\eta), \quad \text{and} \quad \eta\text{can be taken from Eqs (3.4) and (3.5)}, \tag{4.7}$$

where $\Omega(\eta)$ is the wave profile associated with the traveling coordinate η. Substituting the transformation (4.7) into Eq (4.6) converts it into a reduced nonlinear ordinary differential equation of the form

$$F(\Omega, -uv\,\Omega', u\Omega', u^2\Omega'', \dots) = 0. \tag{4.8}$$

To identify analytical solutions, we assume a finite polynomial expansion of $\Omega(\eta)$ in powers of an auxiliary function $f(\eta)$ given by

$$U(\eta) = \sum_{i=0}^{N} B_i\,\Omega^i(\eta), \tag{4.9}$$

where B_i $(i = 0, 1, \dots, N)$ are coefficients to be determined. The first derivative of $\Omega(\eta)$ is assumed to satisfy a first-order ordinary differential equation of the form

$$\Omega'(\eta) = \sqrt{\gamma_1\Omega^4(\eta) + \gamma_2\Omega^2(\eta) + \gamma_3}, \tag{4.10}$$

where γ_1, γ_2, and γ_3 are real parameters controlling the amplitude and shape of the solitary wave.

Soliton and periodic wave structures

Equation (4.2) admits several types of solitary and periodic solutions, which can be represented in terms of Jacobi elliptic functions. Typical examples are summarized below:

$$\begin{cases}
\Omega(\eta) = \mathrm{sn}(\eta) = \tanh(\eta), & \alpha_1 \mapsto m^2,\ \alpha_2 \mapsto -(1+m^2),\ \alpha_3 \mapsto 1, \quad m \to 1^-,\\
\Omega(\eta) = \mathrm{ns}(\eta) = \coth(\eta), & \alpha_1 \mapsto 1,\ \alpha_2 \mapsto -(1+m^2),\ \alpha_3 \mapsto m^2, \quad m \to 1^-,\\
\Omega(\eta) = \mathrm{cn}(\eta) = \mathrm{sech}(\eta), & \alpha_1 \mapsto -m^2,\ \alpha_2 \mapsto 2m^2-1,\ \alpha_3 \mapsto 1-m^2, \quad m \to 1^-,\\
\Omega(\eta) = \mathrm{ds}(\eta) = \mathrm{csch}(\eta), & \alpha_1 \mapsto 1,\ \alpha_2 \mapsto 2m^2-1,\ \alpha_3 \mapsto -m^2(1-m^2), \quad m \to 1^-,\\
\Omega(\eta) = \mathrm{ns}(\eta) \pm \mathrm{ds}(\eta) = \coth(\eta) \pm \mathrm{csch}(\eta), & \alpha_1 \mapsto \frac{1}{4},\ \alpha_2 \mapsto \frac{m^2-2}{2},\ \alpha_3 \mapsto \frac{m^2}{4}, \quad m \to 1^-,\\
\Omega(\eta) = \mathrm{sn}(\eta) \pm i\,\mathrm{cn}(\eta) = \tanh(\eta) \pm i\,\mathrm{sech}(\eta), & \alpha_1 \mapsto \frac{m^2}{4},\ \alpha_2 \mapsto \frac{m^2-2}{2},\ \alpha_3 \mapsto \frac{m^2}{4}, \quad m \to 1^-,\\
\Omega(\eta) = \dfrac{\mathrm{sn}(\eta)}{1 \pm \mathrm{dn}(\eta)} = \dfrac{\tanh(\eta)}{1 \pm \mathrm{sech}(\eta)}, & \alpha_1 \mapsto \frac{m^2}{4},\ \alpha_2 \mapsto \frac{m^2-2}{2},\ \alpha_3 \mapsto \frac{m^2}{4}, \quad m \to 1^-.
\end{cases} \tag{4.11}$$

Here, sn, cn, dn, ns, and ds are Jacobi elliptic functions with elliptic modulus $0 < m < 1$. By substituting Eqs (4.9) and (4.2) into Eq (4.8), one obtains a set of algebraic equations whose solutions yield the constants B_i and determine the physical parameters of the solitary and periodic wave structures.

5. Deriving solutions via the EMETEM

To determine the balancing number N, we balance the highest-order derivative term with the highest nonlinear term in Eq (3.6). $U''(\eta)$ is the highest derivative term, and $U^3(\eta)$ is the highest nonlinear term, which gives $U''(\eta)\zeta^{N+2}$ and $U^3(\eta)\zeta^{3N}$. When these dominant terms are balanced,

$$N + 2 = 3N,$$

which results in $N = 1$. Hence, the trial solution is taken with $N = 1$.

Then, Eq (4.3) takes the form of

$$U(\eta) = M_0 + M_1\zeta(\eta) + N_1[\zeta(\eta)]^{-1}. \tag{5.1}$$

Equations (4.4) and (5.1) can be substituted into Eq (3.6) to provide a polynomial. If we set this form's coefficient to zero, we obtain the system. We only offer the solution set that we used for the graphical representations, even though we obtain several alternative solution sets when we solve the problem.

$$M_0 = \frac{\theta+1}{2}, \quad M_1 = \frac{2\psi}{(\theta+1)\sigma}, \quad N_1 = \frac{(\theta-1)^2(\theta+1)\sigma}{32\psi}$$
$$k = \frac{\sqrt{2}\left(2\theta^2 - 5\theta + 2\right)\psi}{\sqrt{4\theta^6 - 12\theta^5 - 3\theta^4 + 26\theta^3 - 3\theta^2 - 12\theta + 4}\,\sqrt{\sigma}}. \tag{5.2}$$

The values of the unknown variables are entered into Eq (5.1) to produce the family of solitary wave solutions to the governing equation:

Case 1: When $J < 0$,

$$U_1(x,t) = \frac{\theta+1}{2} - \frac{2\sqrt{-J}\psi\tanh\left(\eta\sqrt{-J}\right)}{(\theta+1)\sigma} - \frac{(\theta+1)(\theta-1)^2\sigma\coth\left(\eta\sqrt{-J}\right)}{32\sqrt{-J}\psi}, \tag{5.3}$$

$$U_2(x,t) = \frac{\theta+1}{2} - \frac{(\theta+1)(\theta-1)^2\sigma\tanh\left(\eta\sqrt{-J}\right)}{32\sqrt{-J}\psi} - \frac{2\sqrt{-J}\psi\coth\left(\eta\sqrt{-J}\right)}{(\theta+1)\sigma}, \tag{5.4}$$

$$U_3(x,t) = \frac{\theta+1}{2} - \frac{(\theta+1)(\theta-1)^2\sigma\cosh\left(2\eta\sqrt{-J}\right)}{32\sqrt{-J}\psi\left(\sinh\left(2\eta\sqrt{-J}\right)+i\omega\right)} - \frac{2\sqrt{-J}\psi\,\mathrm{sech}\left(2\eta\sqrt{-J}\right)\left(\sinh\left(2\eta\sqrt{-J}\right)+i\omega\right)}{(\theta+1)\sigma}, \tag{5.5}$$

$$U_4(x,t) = \frac{\theta+1}{2} + \frac{(\theta+1)(\theta-1)^2\sigma\left(\sqrt{-J}\tanh\left(\eta\sqrt{-J}\right)+1\right)}{32\psi\left(J-\sqrt{-J}\tanh\left(\eta\sqrt{-J}\right)\right)} + \frac{2\psi\left(J-\sqrt{-J}\tanh\left(\eta\sqrt{-J}\right)\right)}{(\theta+1)\sigma\left(\sqrt{-J}\tanh\left(\eta\sqrt{-J}\right)+1\right)}, \tag{5.6}$$

$$U_5(x,t) = \frac{\theta+1}{2} + \frac{(\theta+1)(\theta-1)^2\sigma\left(4\sinh\left(2\eta\sqrt{-J}\right)+3\right)}{32\sqrt{-J}\psi\left(5-4\cosh\left(2\eta\sqrt{-J}\right)\right)} + \frac{2\sqrt{-J}\psi\left(5-4\cosh\left(2\eta\sqrt{-J}\right)\right)}{(\theta+1)\sigma\left(4\sinh\left(2\eta\sqrt{-J}\right)+3\right)}, \tag{5.7}$$

$$U_6(x,t) = \frac{\theta+1}{2} + \frac{(\theta+1)(\theta-1)^2\sigma\left(m\sinh\left(2\eta\sqrt{-J}\right)+n\right)}{32\psi\left(\omega\sqrt{-J\left(m^2+n^2\right)}-\sqrt{-J}m\cosh\left(2\eta\sqrt{-J}\right)\right)} + \frac{2\psi\left(\omega\sqrt{-J\left(m^2+n^2\right)}-\sqrt{-J}m\cosh\left(2\eta\sqrt{-J}\right)\right)}{(\theta+1)\sigma\left(m\sinh\left(2\eta\sqrt{-J}\right)+n\right)}, \tag{5.8}$$

$$U_7(x,t)=\frac{\theta+1}{2}+\frac{(\theta+1)(\theta-1)^2\sigma}{32\sqrt{-J}\psi\omega\left(1-\frac{2m}{-\omega\sinh\left(2\eta\sqrt{-J}\right)+\cosh\left(2\eta\sqrt{-J}\right)+m}\right)}+\frac{2\sqrt{-J}\psi\omega\left(1-\frac{2m}{-\omega\sinh\left(2\eta\sqrt{-J}\right)+\cosh\left(2\eta\sqrt{-J}\right)+m}\right)}{(\theta+1)\sigma}. \tag{5.9}$$

Case 2: When $J>0$,

$$U_8(x,t)=\frac{\theta+1}{2}+\frac{2\sqrt{J}\psi\tan\left(\eta\sqrt{J}\right)}{(\theta+1)\sigma}+\frac{(\theta+1)(\theta-1)^2\sigma\cot\left(\eta\sqrt{J}\right)}{32\sqrt{J}\psi}, \tag{5.10}$$

$$U_9(x,t)=\frac{\theta+1}{2}-\frac{(\theta+1)(\theta-1)^2\sigma\tan\left(\eta\sqrt{J}\right)}{32\sqrt{J}\psi}-\frac{2\sqrt{J}\psi\cot\left(\eta\sqrt{J}\right)}{(\theta+1)\sigma}, \tag{5.11}$$

$$U_{10}(x,t)=\frac{\theta+1}{2}+\frac{(\theta+1)(\theta-1)^2\sigma\cos\left(2\eta\sqrt{J}\right)}{32\sqrt{J}\psi\left(\sin\left(2\eta\sqrt{J}\right)+\omega\right)}+\frac{2\sqrt{J}\psi\sec\left(2\eta\sqrt{J}\right)\left(\sin\left(2\eta\sqrt{J}\right)+\omega\right)}{(\theta+1)\sigma}, \tag{5.12}$$

$$U_{11}(x,t)=\frac{\theta+1}{2}-\frac{(\theta+1)(\theta-1)^2\sigma\left(\tan\left(\eta\sqrt{J}\right)+1\right)}{32\sqrt{J}\psi\left(1-\tan\left(\eta\sqrt{J}\right)\right)}-\frac{2\sqrt{J}\psi\left(1-\tan\left(\eta\sqrt{J}\right)\right)}{(\theta+1)\sigma\left(\tan\left(\eta\sqrt{J}\right)+1\right)}, \tag{5.13}$$

$$U_{12}(x,t)=\frac{\theta+1}{2}-\frac{(\theta+1)(\theta-1)^2\sigma\left(5\sin\left(2\eta\sqrt{J}\right)+3\right)}{32\sqrt{J}\psi\left(4-5\cos\left(2\eta\sqrt{J}\right)\right)}-\frac{2\sqrt{J}\psi\left(4-5\cos\left(2\eta\sqrt{J}\right)\right)}{(\theta+1)\sigma\left(5\sin\left(2\eta\sqrt{J}\right)+3\right)}, \tag{5.14}$$

$$U_{13}(x,t)=\frac{\theta+1}{2}+\frac{2\psi\left(\omega\sqrt{J\left(m^2-n^2\right)}-\sqrt{J}m\cos\left(2\eta\sqrt{J}\right)\right)}{(\theta+1)\sigma\left(m\sin\left(2\eta\sqrt{J}\right)+n\right)}- \tag{5.15}$$

$$+\frac{(\theta+1)(\theta-1)^2\sigma\left(m\sin\left(2\eta\sqrt{J}\right)+n\right)}{32\psi\left(\omega\sqrt{J\left(m^2-n^2\right)}-\sqrt{J}m\cos\left(2\eta\sqrt{J}\right)\right)}, \tag{5.16}$$

$$U_{14}(x,t)=\frac{\theta+1}{2}+\frac{2i\sqrt{J}\psi\omega\left(1-\frac{2m}{-i\omega\sin\left(2\eta\sqrt{J}\right)+\cos\left(2\eta\sqrt{J}\right)+m}\right)}{(\theta+1)\sigma}-\frac{i(\theta+1)(\theta-1)^2\sigma}{32\sqrt{J}\psi\omega\left(1-\frac{2m}{-i\omega\sin\left(2\eta\sqrt{J}\right)+\cos\left(2\eta\sqrt{J}\right)+m}\right)}. \tag{5.17}$$

Case 3: When $J=0$,

$$U_{15}(x,t)=-\frac{(\theta+1)(\theta-1)^2\eta\sigma}{32\psi}-\frac{2\psi}{(\theta+1)\eta\sigma}+\frac{\theta+1}{2}. \tag{5.18}$$

5.1. Extraction of analytical solutions via F-expansion method

By applying the balancing technique in Eq (3.6), we arrive at $N = 1$. Equation (4.9) takes the form

$$U(\eta) = B_0 + B_1\Omega(\eta). \tag{5.19}$$

The system of equations is obtained by substituting Eqs (5.19) and (4.10) into Eq (3.6). This system of equations is then solved to obtain the following results:

$$\gamma_1 = -\frac{2\sigma^2 B_0^4}{\psi^2}, \quad \gamma_3 = \frac{\sigma^4 B_0^8}{\gamma_1 \psi^4}, \quad k = \frac{\sqrt{2}\,\psi}{2\sqrt{\sigma}\,B_0}, \quad \theta = 2B_0 - 1, \quad B_1 = \frac{\sqrt{P}\,\psi}{B_0\sigma}. \tag{5.20}$$

We can manipulate algebraically to obtain the soliton solution in its exact form by combining Eq (5.20) into Eq (5.19). The following circumstances are used to categorize the response.

Case 1: When $\Omega(\eta) = \mathrm{sn}(\eta) = \tanh(\eta)$, $\gamma_1 = m^2$, $\gamma_2 = -(1 + m^2)$, $\gamma_3 = 1$.

$$U_{16}(x,t) = B_0 + \frac{\psi \tanh(\eta)}{B_0\sigma}. \tag{5.21}$$

Case 2: When $\Omega(\eta) = \mathrm{ns}(\eta) = \coth(\eta)$, $\gamma_1 = 1$, $\gamma_2 = -(1 + m^2)$, $\gamma_3 = m^2$.

$$U_{17}(x,t) = B_0 + \frac{\psi \coth(\eta)}{B_0\sigma}. \tag{5.22}$$

Case 3: When $\Omega(\eta) = \mathrm{cn}(\eta) = \mathrm{sech}(\eta)$, $\gamma_1 = -m^2$, $\gamma_2 = 2m^2 - 1$, $\gamma_3 = 1 - m^2$.

$$U_{18}(x,t) = B_0 + \frac{\mathrm{i}\psi \mathrm{sech}(\eta)}{2B_0\sigma}. \tag{5.23}$$

Case 4: When $\Omega(\eta) = \mathrm{ds}(\eta) = \mathrm{csch}(\eta)$, $\gamma_1 = 1$, $\gamma_2 = 2m^2 - 1$, $\gamma_3 = -m^2(1 - m^2)$.

$$U_{19}(x,t) = B_0 + \frac{\psi \,\mathrm{csch}(\eta)}{B_0\sigma}. \tag{5.24}$$

Case 5: When $\Omega(\eta) = \mathrm{ns}(\eta) \pm \mathrm{ds}(\eta) = \coth(\eta) \pm \mathrm{csch}(\eta)$, $\gamma_1 = \frac{1}{4}$, $\gamma_2 = \frac{m^2-2}{2}$, $\gamma_3 = \frac{m^2}{4}$.

$$U_{20}(x,t) = B_0 + \frac{\psi\,(\coth(\eta) + \mathrm{csch}(\eta))}{2B_0\sigma}, \tag{5.25}$$

$$U_{21}(x,t) = B_0 + \frac{\psi\,(\coth(\eta) - \mathrm{csch}(\eta))}{2B_0\sigma}. \tag{5.26}$$

Case 6: When $\Omega(\eta) = \mathrm{sn}(\eta) \pm \mathrm{icn}(\eta) = \tanh(\eta) \pm \mathrm{isech}(\eta)$, $\gamma_1 = \frac{m^2}{4}$, $\gamma_2 = \frac{m^2-2}{2}$, $\gamma_3 = \frac{m^2}{4}$.

$$U_{22}(x,t) = B_0 + \frac{\psi\,(\tanh(\eta) + \mathrm{i}\,\mathrm{sech}(\eta))}{2B_0\sigma}, \tag{5.27}$$

$$U_{23}(x,t) = B_0 + \frac{\psi\left(\tanh(\eta) - \mathrm{i}\,\mathrm{sech}(\eta)\right)}{2B_0\sigma}. \tag{5.28}$$

Case 7: When $\Omega(\eta) = \frac{\mathrm{sn}(\eta)}{1\pm\mathrm{dn}(\eta)} = \frac{\tanh(\eta)}{1\pm\mathrm{sech}}$, $\gamma_1 = \frac{m^2}{4}$, $\gamma_2 = \frac{m^2-2}{2}$, $\gamma_3 = \frac{m^2}{4}$.

$$U_{24}(x,t) = B_0 + \frac{\psi\tanh(\eta)}{2B_0\sigma\left(1+\mathrm{sech}(\eta)\right)}, \tag{5.29}$$

$$U_{25}(x,t) = B_0 + \frac{\psi\tanh(\eta)}{2B_0\sigma\left(1-\mathrm{sech}(\eta)\right)}. \tag{5.30}$$

6. Graphical analysis and physical interpretation

This section presents the graphical analysis of the fractional Huxley model constructed using both the β-derivative and the M-truncated fractional derivative. To clearly relate the analytical results obtained from Eq (3.6) back to the original fractional Huxley model (3.1), we present graphical representations of the solutions in terms of the original variables. The transformations in (3.4) and (3.5) provide a direct mapping from the ordinary differential equation (ODE) solutions to the spatiotemporal profiles of $U(x,t)$ in Eq (3.1). Figures are plotted for both the M-truncated fractional derivative and the β-fractional derivative to illustrate the distinct effects of the two operators on wave amplitude, width, and propagation. This visual comparison not only confirms the validity of analytical solutions but also reinforces the correspondence between ODE-based analysis and the original fractional PDE model, addressing the connection between subsequent results and Eq (3.1). The analytical solutions obtained in the preceding sections are visualized for several values of the fractional order parameters to examine how the order of differentiation and truncation degree affect the system's nonlinear wave dynamics. Each figure illustrates the temporal and spatial evolution of the wave profile, revealing the intrinsic link between the fractional calculus operators and the corresponding dispersive-nonlinear balance. It is important to emphasize that, for the present β-fractional and M-truncated formulations, the fractional order δ enters the solution only through the traveling variable η. Consequently, varying δ primarily induces a phase shift and spatial rescaling of the waveform, whereas the peak amplitude, which is determined by the reduced ordinary differential equation, remains invariant.

Figures 1 and 2 display the three- and two-dimensional plots of the solution $U_3(x,t)$ associated with Eq (5.5). The $3D$ surface illustrates the smooth propagation of a localized soliton-type structure that retains its integrity as it travels along the spatial axis. The $2D$ profiles demonstrate that varying δ mainly affects the spatial position and localization of the soliton, and the peak amplitude remains unchanged. Higher fractional orders yield sharper and more confined wave fronts due to enhanced nonlinear dispersive balance. For smaller δ, the soliton broadens and exhibits a gentler slope, corresponding to weaker nonlinear interactions. Together, the $3D$ and $2D$ plots provide a clear visualization of how the fractional operator modulates the stability and localization of the wave structure.

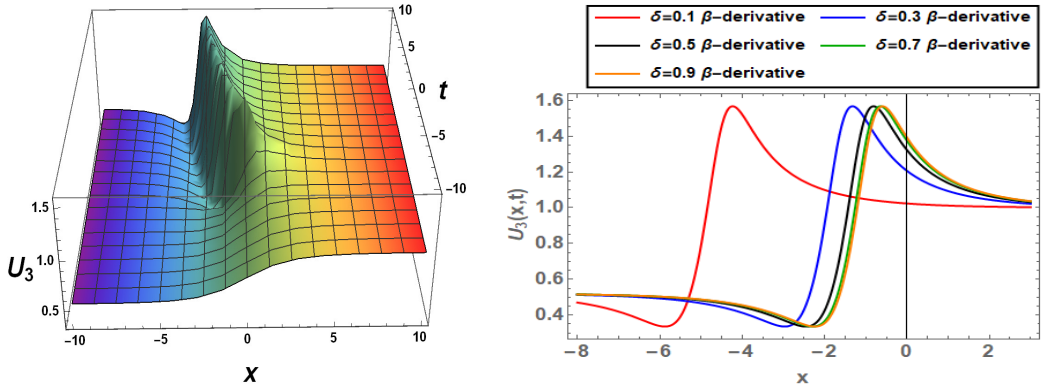

Figure 1. The three-dimensional ($3D$) and two-dimensional ($2D$) profiles of the solution $U_3(x,t)$ using the parametric values $\omega = 0.1$, $\theta = 0.52$, $\psi = -0.9$, $\sigma = 0.4$, $k = 2$, and $\delta = 0.5$. It is observed that increasing δ results in sharper and more localized peaks, indicating stronger nonlinear and dispersive effects. The $3D$ surface illustrates a soliton-like structure that propagates whereas preserving its shape, whereas the $2D$ profiles show that variations in the fractional order primarily affect the spatial position and localization of the wave, with the peak amplitude remaining essentially unchanged.

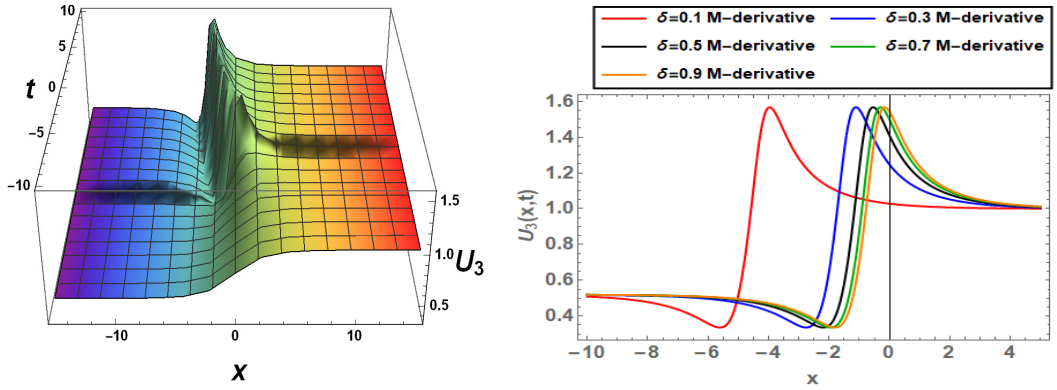

Figure 2. The $3D$ surface demonstrates a soliton-like structure that maintains its shape during propagation, for the parametric values $\omega = 0.1$, $\theta = 0.52$, $\psi = -0.9$, $\sigma = 0.4$, $k = 2$, $\rho = 1.5$, and $\delta = 0.5$, whereas the $2D$ plot highlights how the fractional derivative order affects the amplitude and width of the waveform. The results demonstrate that increasing δ leads to sharper and more localized wave fronts, whereas the maximum amplitude remains invariant, indicating that the fractional order mainly modulates propagation characteristics rather than amplitude.

Figures 3 and 4 correspond to the solution $U_{12}(x,t)$. The $3D$ surface describes the temporal–spatial propagation of a soliton-like structure, whereas the $2D$ cross-section compares the amplitude response under varying fractional orders of both β and M. An increase in δ results in a noticeable horizontal shift and steepening of the wave front, whereas the maximum amplitude remains effectively constant. This confirms that the fractional order modulates propagation characteristics rather than energy level. The plots highlight how the M-truncated operator reproduces the main features of the β-derivative whereas introducing subtle damping and shape-retaining effects that enhance wave stability.

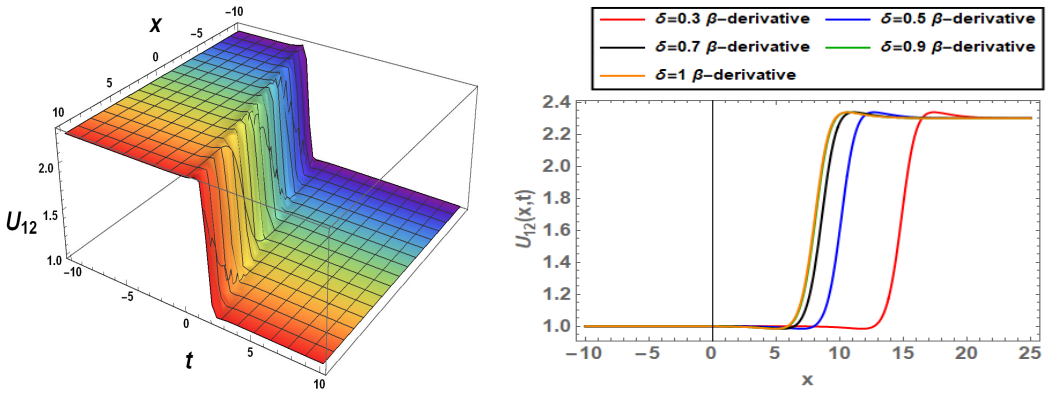

Figure 3. The $3D$ and $2D$ plots of the solution $U_{12}(x,t)$ using the parametric values $\theta = 2.3$, $\psi = 1$, $\sigma = 1.4$, $k = 0.24$, and $\delta = 1$. The $2D$ plots compare wave profiles for different fractional orders, revealing that variations in δ primarily induce horizontal shifts and changes in localization, whereas the peak amplitude remains nearly constant.

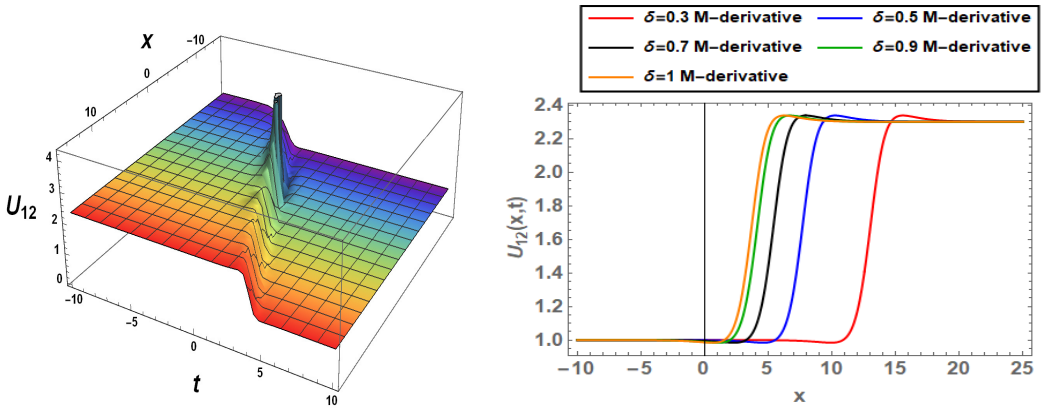

Figure 4. The $3D$ and $2D$ plots for Eq. (5.14) are shown using the parametric values $\theta = 2.3$, $\psi = 1$, $\sigma = 1.4$, $k = 0.24$, $\rho = 1.5$, and $\delta = 0.1$. The wave maintains its soliton-like structure, and the $2D$ profiles confirm that fractional-order variation affects the spatial transition and steepness of the waveform without significant change in amplitude.

Figures 5 and 6 illustrate the $3D$ and $2D$ profiles of the solution $U_{18}(x,t)$. The $3D$ surface reveals a symmetric bell-shaped soliton that propagates stably without distortion. From the corresponding $2D$ cross-sections, it is observed that varying the fractional order δ primarily affects the localization and width of the soliton. As δ increases, the waveform becomes more confined and sharper around its center, whereas the peak amplitude remains nearly unchanged. This indicates that, for this solution, the fractional order mainly regulates spatial localization rather than producing a significant amplification of the wave height. The near-invariance of the maximum amplitude is consistent with the analytical structure of the reduced ordinary differential equation, in which the fractional order δ enters through the traveling coordinate rather than the amplitude-determining coefficients.

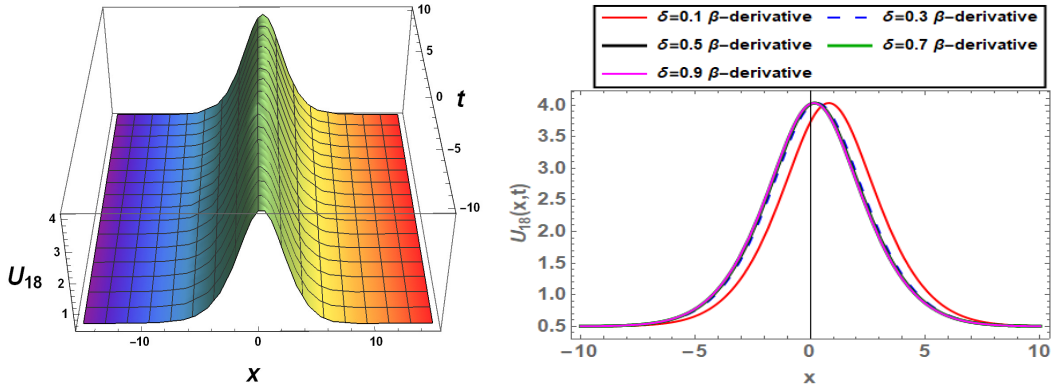

Figure 5. $3D$ and $2D$ plots of the solution $U_{18}(x,t)$ with $B_0 = 0.5$, $\psi = 0.04$, $\sigma = 0.01$, $k = 0.5$, and $\delta = 0.3$. Increasing the fractional order δ leads to enhanced localization and narrowing of the soliton profile, whereas the peak amplitude remains nearly unchanged.

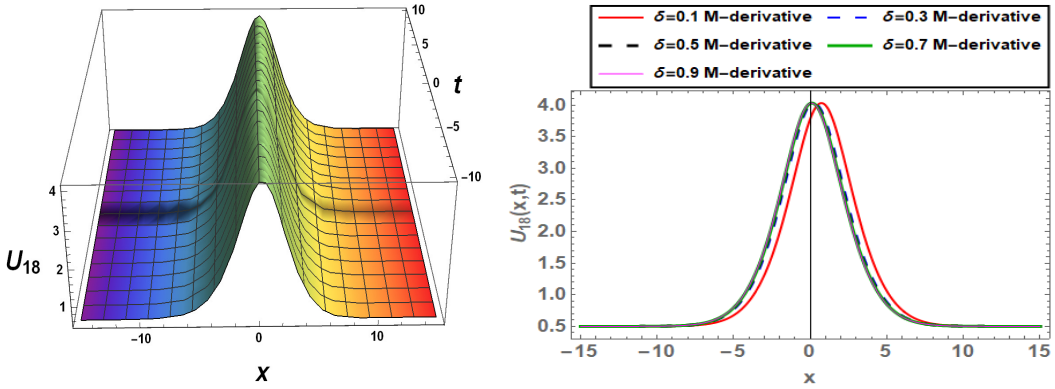

Figure 6. The $3D$ and $2D$ plots of the solution $U_{18}(x,t)$ obtained using the M-truncated fractional derivative for the same parameter values as in Fig. 5. The comparison shows that the M-truncated operator preserves the bell-shaped soliton structure and yields similar localization behavior, with minimal variation in peak amplitude across different fractional orders.

Figures 7 and 8 represent the solution $U_{22}(x,t)$ obtained for Eq (5.27). The $3D$ plots depict an inverted, trough-shaped soliton whose depth and localization increase with higher fractional orders. As δ grows, the soliton well becomes deeper and more pronounced, indicating that stronger fractional effects intensify the nonlinear steepening of the waveform. The corresponding $2D$ graphs confirm this trend: the peak-to-valley difference widens with increasing δ, illustrating the transition from a smooth to a sharply localized structure. When the same parameters are applied to the M-truncated derivative, the soliton remains stably inverted but exhibits slightly smoother edges, suggesting that the truncation introduces a regularizing influence that counteracts excessive steepening. As δ increases, the inverted soliton becomes narrower and more pronounced in depth, indicating stronger localization effects, whereas the extremal values remain bounded within the same amplitude range.

The observed invariance of peak amplitude with respect to the fractional order δ is a direct consequence of the β-fractional and M-truncated traveling-wave transformations, where δ appears solely in the phase variable. As a result, fractional differentiation influences the spatial–temporal

distribution and localization of the wave rather than its energy level. This behavior is consistent with the structure of the reduced ODE and confirms that fractional effects primarily regulate propagation dynamics instead of amplitude amplification. All analytical and numerical figures in Sections 6 and 7 are plotted using identical spatial and temporal intervals to allow direct visual comparison.

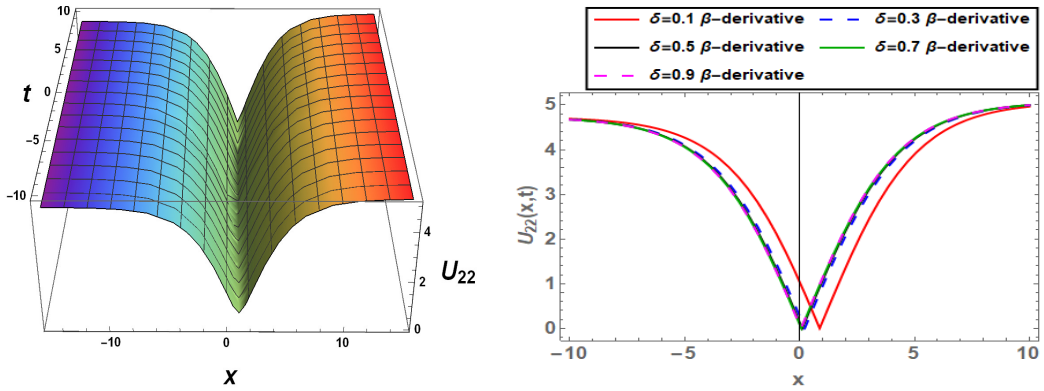

Figure 7. $3D$ and $2D$ plots of the solution $U_{22}(x,t)$ for Eq. (5.27) for values $B_0 = 0.17$, $\psi = 0.05$, $\sigma = 0.03$, $k = 0.5$, and $\delta = 0.1$. The solution represents an inverted soliton structure whose width and depth are influenced by the fractional order, whereas the extremal amplitude remains bounded.

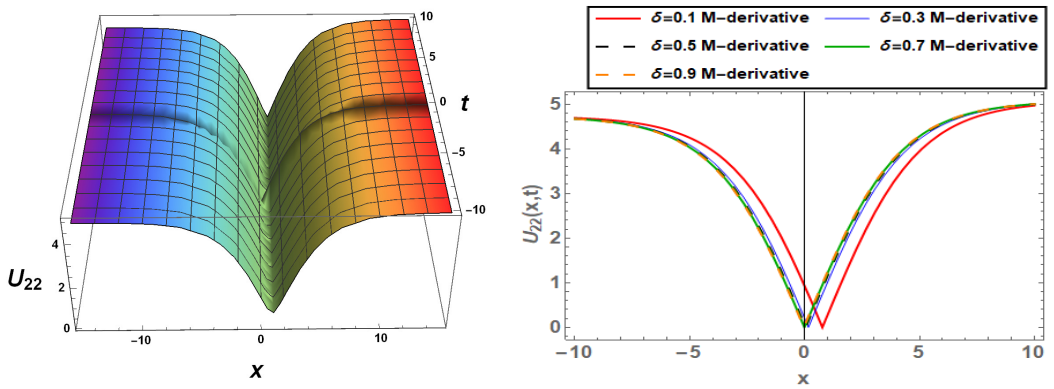

Figure 8. The $3D$ and $2D$ plots of the solution $U_{22}(x,t)$ obtained using the M-truncated fractional derivative for the same parameters as in Figure 7. The results show that increasing the fractional order leads to a more localized and pronounced inverted soliton profile, with the overall amplitude remaining nearly invariant.

7. Finite difference numerical validation

It is important to clarify the relationship between numerical simulations presented in Sections 6 and 7. The analytical solutions derived from Eq (3.6) are graphically shown in Section 6, showing how the M-truncated and β-fractional derivatives affect wave amplitude, width, and shape. In contrast, Section 7 implements a finite-difference-based numerical scheme directly on the original fractional Huxley equation (3.1) without using ODE transformation. This enables the analytical solutions to be verified and shows that the numerical approach for the original PDE is accurate, stable, and consistent.

To validate the analytical solutions, a representative finite-difference discretization is employed using the same spatial and temporal domains as those used in Section 6. Other standard finite-difference variants yield qualitatively similar behavior and are therefore omitted from the main text to streamline presentation and focus on analytical-numerical agreement.

To complement the analytical investigation, the governing equation is solved numerically using a finite difference approach. In this study, we employ the forward-centered difference scheme (F-CDS) as a representative and stable discretization for validating the analytical solutions.

Expanding the function $P(x)$ in a Taylor series yields

$$P(x+a) = P(x) + aP'(x) + \frac{a^2}{2!}P''(x) + \cdots . \tag{7.1}$$

The first- and second-order derivatives can then be approximated as

$$P'(x) \approx \frac{P(x+a) - P(x)}{a}, \tag{7.2}$$

$$P''(x) \approx \frac{P(x+a) - 2P(x) + P(x-a)}{a^2}. \tag{7.3}$$

7.1. Forward-centered difference scheme

The F-CDS utilizes a forward stencil in time and a centered stencil in space. This combination provides a balanced compromise between computational efficiency and accuracy, minimizing numerical dispersion in wave-like solutions. From Taylor's expansion, the finite difference formulas are expressed as

$$P_x \approx \frac{P(x+a,t) - P(x,t)}{a}, \tag{7.4}$$

$$P_{xx} \approx \frac{P(x+a,t) - 2P(x,t) + P(x-a,t)}{a^2}, \tag{7.5}$$

$$P_t \approx \frac{P(x,t+b) - P(x,t)}{b}, \tag{7.6}$$

$$P_{tt} \approx \frac{P(x,t+b) - 2P(x,t) + P(x,t-b)}{b^2}. \tag{7.7}$$

Substituting Eqs (7.4)–(7.7) into Eq (3.1) leads to the discrete form

$$P_{i,j+1} = \frac{bP_{i+1,j}}{a^2} + \left(-\frac{2b}{a^2} - b\sigma\theta + 1\right)P_{i,j} + (b\sigma\theta + b\sigma)\,P_{i,j}^2 + \frac{bP_{i-1,j}}{a^2} - b\sigma P_{i,j}^3. \tag{7.8}$$

By introducing the coefficients

$$\alpha_1 = \frac{b}{a^2}, \quad \alpha_2 = \left(-\frac{2b}{a^2} - b\sigma\theta + 1\right), \quad \alpha_3 = (b\sigma\theta + b\sigma), \quad \alpha_4 = \frac{b}{a^2}, \quad \alpha_5 = -b\sigma,$$

the updated equation can be written compactly as

$$P_{i,j+1} = \alpha_1 P_{i+1,j} + \alpha_2 P_{i,j} + \alpha_3 P_{i,j}^2 + \alpha_4 P_{i-1,j} + \alpha_5 P_{i,j}^3. \tag{7.9}$$

Figure 9 presents the numerical surface generated using the F-CDS, depicting the evolution of $P(x, t)$ across the spatial-temporal domain.

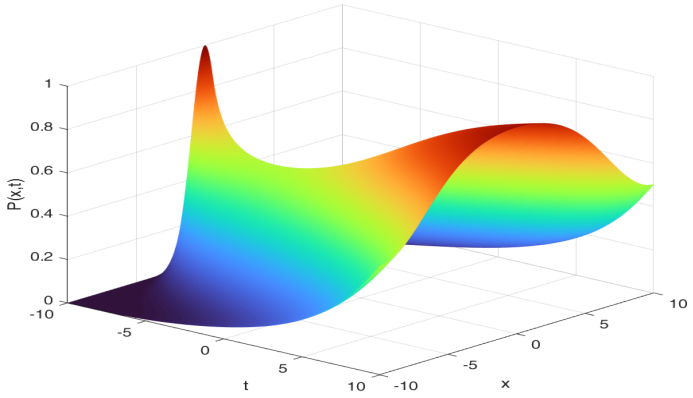

Figure 9. Three-dimensional surface plot of $P(x, t)$ obtained using the F-CDS. The method accurately reproduces the nonlinear spatiotemporal dynamics, capturing both amplitude and phase variations of the evolving wave.

The numerical surface in Figure 9 reproduces the same soliton profile, localization, and bounded amplitude observed in the analytical plots of Section 6 under identical parameter values. The solutions obtained through the analytical method exhibit smooth and consistent wave behavior and capture the essential dynamics of the fractional Huxley equation. Similarly, the solutions obtained through the numerical method follow the same general trends and profiles over the considered spatial and temporal domains. A pointwise comparison between the two solutions shows that the differences remain very small throughout the computational domain, indicating good agreement between the analytical and numerical approaches. Any minor deviations can be attributed to discretization effects. Further study will continue by applying more advanced numerical techniques to investigate error behavior in greater detail.

8. Bifurcation analysis

In this section, we provide the bifurcation analysis of the model under study to examine how parameter changes impact the qualitative behavior of solutions. The research pinpoints the critical times when the stability and dynamical structure of the system shift. Such an analysis insightfully illustrates both the model's sensitivity and the emergence of different solution patterns under parameter modifications.

To investigate the bifurcation features of the nonlinear governing equation, we reformulate it into an equivalent planar dynamical system, which is given by

$$\begin{cases} \dfrac{dU}{d\eta} = \phi, \\ \dfrac{d\phi}{d\eta} = aU^3 + bU^2 + cU + d\phi, \end{cases} \tag{8.1}$$

where

$$a = \frac{\sigma}{k^2}, \quad b = -\frac{\sigma(1+\theta)}{k^2}, \quad c = \frac{\sigma\theta}{k^2}, \quad = -\frac{\psi}{k^2}.$$

The system's Jacobian matrix, represented by $\mathcal{J}(U,\phi)$ is used to analyze its stability. It is defined as follows:

$$\mathcal{J}(U,\phi) = \begin{pmatrix} 0 & 1 \\ 3U^2 + 2bU + c & d \end{pmatrix}. \tag{8.2}$$

The determinant of the Jacobian matrix can be expressed as

$$\det \mathcal{J}(U,\phi) = -(3U^2 + 2bU + c). \tag{8.3}$$

The character of the equilibrium point at $\phi = 0$ is identified through $\det \mathcal{J}(U,0)$, namely

$$\text{Equilibrium type} = \begin{cases} \text{Center}, & \det \mathcal{J}(U,0) > 0, \\ \text{Saddle}, & \det \mathcal{J}(U,0) < 0, \\ \text{Cusp}, & \det \mathcal{J}(U,0) = 0. \end{cases}$$

Thus, the system possesses three distinct equilibrium states.

$$E_1 = (0,0), \quad E_{2,3} = \left(\frac{-b \pm \sqrt{b^2 - 4ac}}{2a}, 0 \right).$$

The bifurcation possibilities of the system under parameter variations are largely determined by these equilibria. This raises the following potential outcomes:

- For $a > 0$, $b > 0$, $c > 0$, and $d > 0$, each of the three equilibrium points shows saddle. The system's bifurcation structure and the various kinds of equilibrium states are depicted in the phase portrait above. Three red-marked saddle points are located at $(-3,0)$, $(0,0)$, and $(2,0)$. Trajectories are directed either towards or away from the saddles by their separatrices, which are represented by black curves and divide the phase plane into discrete dynamical regions. On the other hand, spiral trajectories (shown in blue and magenta) in the middle region show oscillatory behavior surrounding the equilibrium. The phase portrait has been illustrated in Figure 10.

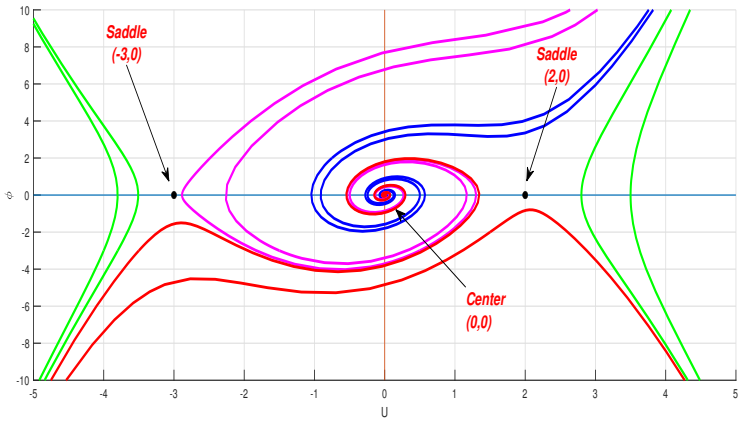

Figure 10. Phase portrait illustrating the bifurcation structure of the dynamical system in the (U,ϕ) plane with the values $a = 1$, $b = 1$, $c = 6$, and $d = 1$.

- For $a < 0$, $b > 0$, $c > 0$, and $d > 0$, the plot highlights three equilibrium points: a center at each $(-0.5, 0)$ and $(1, 0)$ and a saddle at $(0, 0)$. Contour curves illustrate the system's stability structure, where trajectories near the center exhibit oscillatory behavior, whereas those near the saddle diverge along unstable directions. The qualitative analysis has been computed and illustrated in Figure 11.

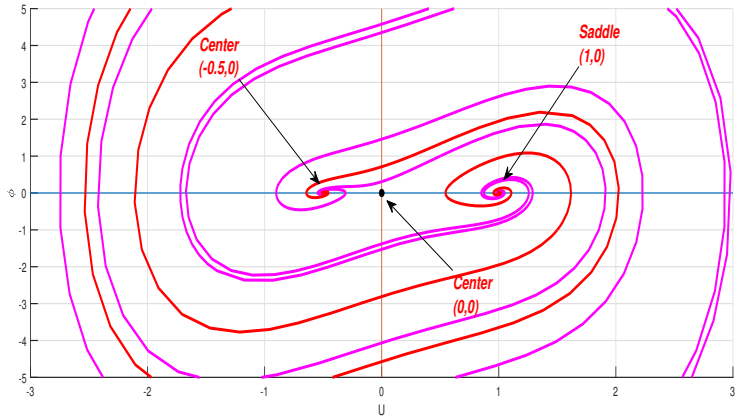

Figure 11. Phase portrait with contour lines showing equilibrium points in a nonlinear dynamical system.

- For $a > 0$, $b > 0$, $c < 0$, and $d > 0$, three critical locations are indicated: two saddles in $(-5, 0)$ and $(4, 0)$ and a center in $(0, 0)$. Stable oscillatory behavior is shown by the closed orbits surrounding the center. Figure 12 shows the portrait for this case.

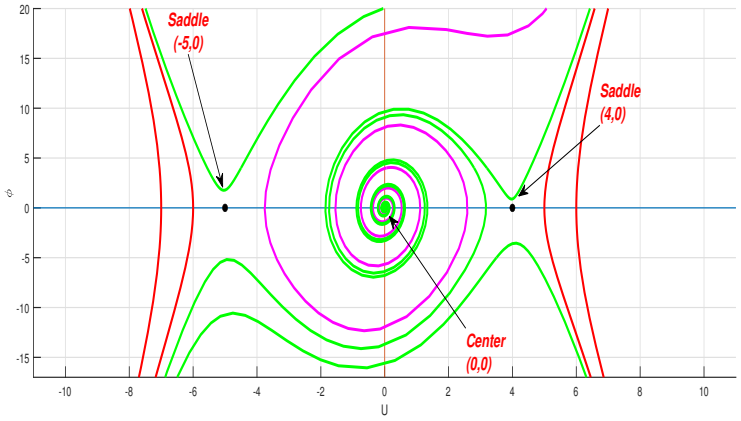

Figure 12. Phase portrait with contour lines showing equilibrium points in a nonlinear dynamical system.

It is worth noting that the qualitative transitions observed in the first three cases correspond to codimension-1 bifurcations driven by variations in a single control parameter (such as a, c, or d). In particular, changes in the sign of $\det \mathcal{J}(U, \phi)$ and the associated eigenvalue structure of the Jacobian matrix lead to saddle–center and center–saddle transitions in the phase plane. These transitions mark the onset or disappearance of closed orbits and separatrix structures and are

characteristic of codimension-1 bifurcation behavior. Thus, although explicit bifurcation diagrams are not presented, the analytical phase-plane analysis provides a rigorous theoretical characterization of the underlying bifurcation mechanisms.

- For $a > 0$, $b > 0$, $c < 0$, and $d = 0$, this dynamical system's contour map displays equilibrium points. Whereas $(-2, 0)$, and $(1, 0)$ are saddle points connected by separatrices that separate regions of motion, the origin $(0, 0)$ is a center encircled by closed orbits. Figure 13 presents the phase portrait corresponding to the chosen set of parameters.

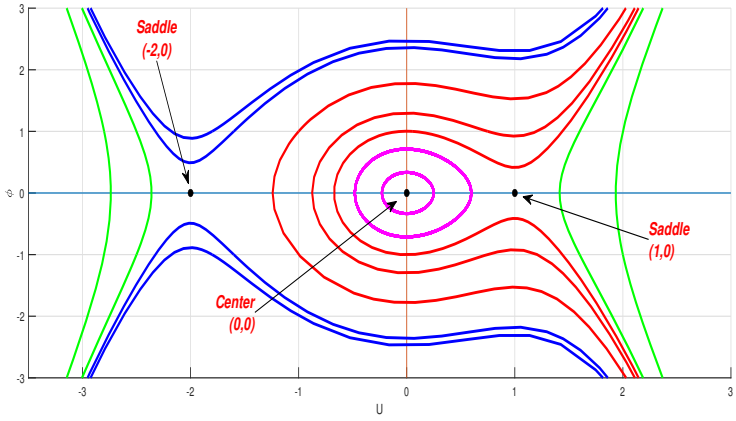

Figure 13. Contour plot of a dynamical system showing equilibrium points.

- For $a < 0$, $b > 0$, $c > 0$, and $d = 0$, this dynamical system's contour map displays equilibrium points. Whereas $(2, 0)$, and $(-1, 0)$ are centers, the origin $(0, 0)$ is a saddle. As shown in Figure 14, the phase portrait depicts the system's behavior for this specific parameter set.

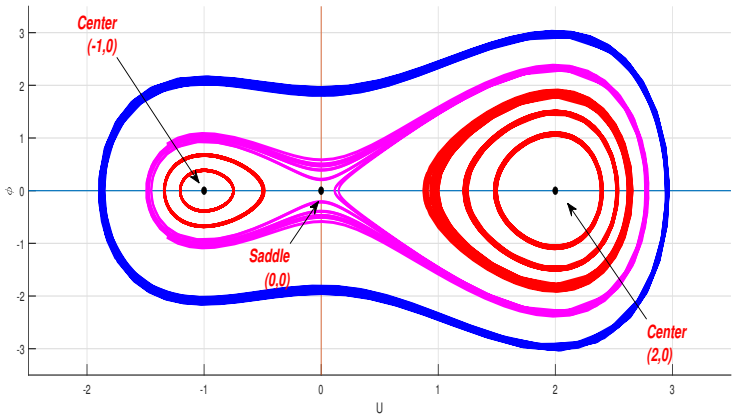

Figure 14. Phase portrait illustrating two centers and a saddle.

- For $a = 0$, $b > 0$, $c > 0$, and $d = 0$, the plot illustrates the phase space trajectories with a center at $(-1, 0)$ surrounded by closed orbits and a saddle at $(0, 0)$ showing diverging and converging paths. It highlights the contrast between stable periodic motion and unstable behavior. Figure 15 shows the phase portrait for this case, highlighting the qualitative dynamics for this case.

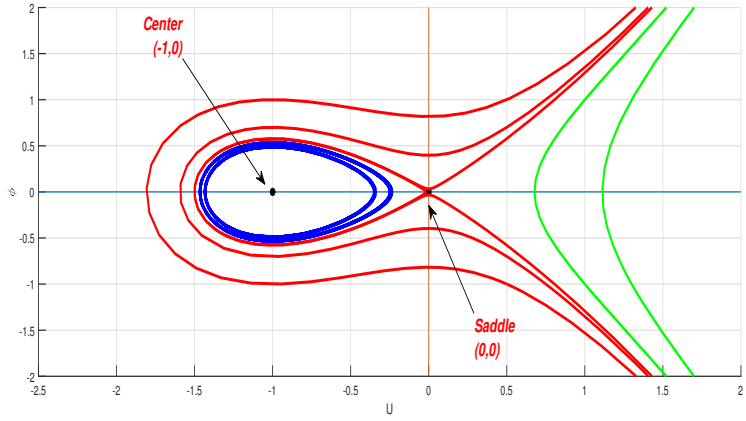

Figure 15. Phase portrait showing stable and unstable dynamics.

The bifurcation behavior of the fractional Huxley equation is investigated through phase-plane analysis for selected parameter values. By varying key system parameters whereas keeping others fixed, qualitative changes in the dynamical structure are observed in the form of transitions between stable and unstable equilibrium states, as well as variations in the shape and orientation of trajectories. The phase portraits illustrate how the solution trajectories evolve under parameter changes, revealing the influence of fractional order and nonlinear terms on system stability. These observations provide insight into the local dynamical behavior of the system and demonstrate the sensitivity of the solution structure to parameter variations.

A natural extension of the present study is to perform a systematic bifurcation analysis by constructing codimension-1 and codimension-2 bifurcation diagrams through numerical continuation techniques. Such an approach would allow a more comprehensive understanding of the global dynamical behavior of the system and the interaction between multiple control parameters.

9. Conclusions

The β-fractional derivative and the M-truncated derivative are two nonlocal operators that we used in this work to create a thorough framework for studying the higher-order nonlinear fractional Huxley model. By combining the F-expansion procedure with the enhanced modified extended tanh expansion method, a rich catalogue of exact solutions was derived, including soliton profiles, trigonometric forms, and families expressed through single and combined Jacobi elliptic functions. These closed-form results clarify how fractional memory modifies wave amplitude, width, and propagation characteristics, and they provide reusable templates for related nonlinear models in mathematical physics. The two operators exhibited complementary behaviors when compared head-to-head. The β-fractional derivative tends to localize and sharpen waveforms, indicating that it can be used to mimic highly localized biological events or fast signal propagation, and the M-truncated operator yields shape-preserving profiles with mild regularization due to the truncation of the memory tail. These trends are consistent across the solution families reported here and give practical guidance for selecting an operator to match a target physical regime. These results offer useful recommendations for choosing suitable operators to represent different biological regimes.

To corroborate the analytical results, a finite-difference-based numerical scheme was developed

and applied to the fractional Huxley equation. The obtained numerical surfaces closely followed the analytical predictions, demonstrating the accuracy, consistency, and stability of the proposed approach. In parallel, a qualitative investigation based on planar dynamical systems exposed parameter windows that govern transitions between distinct regimes. The phase portraits exhibit stable and unstable spiral-type bifurcations and demonstrate how frequency and amplitude parameters steer the system between localized, periodic, and mixed behaviors. Phase pictures revealed stable and unstable spiral-type bifurcations, clarifying how amplitude and frequency parameters control excitability and stability. These findings are directly applicable to comprehending the propagation of brain or cardiac signals in biological tissues. This study presents multiple analytical solutions of the fractional Huxley model with results validated through a finite difference scheme. The bifurcation analysis provides a deeper understanding of the system's qualitative dynamics and stability. Overall, this work demonstrates the effectiveness of combining analytical and numerical approaches, underscores the significance of fractional-order formulation in capturing memory effects and complex nonlinear behaviors that are absent in classical models.

Future research directions include the development of energy-based stability criteria for the reported waves, data-driven operator learning to infer effective fractional orders from experimental observations, extensions to higher-dimensional and anisotropic systems, and the incorporation of stochastic forcing to explore robustness under physiological variability and uncertainty. These paths will help close the gap between biological occurrences in the real world and quantitative models. Furthermore, a more detailed comparison between analytical and numerical solutions will be carried out by evaluating pointwise errors and standard error norms to further assess numerical accuracy. In addition, a systematic analysis based on codimension-1 and -2 bifurcation diagrams, obtained through numerical continuation techniques, will be considered. Such investigations would provide deeper insight into the global dynamical behavior of the system and interplay between multiple control parameters.

Author contributions

All authors contributed equally to the preparation of this manuscript. All authors have read and approved the final version of the manuscript for publication.

Use of Generative-AI tools declaration

The authors declare they have not used Artificial Intelligence tools in the creation of this article.

Funding

This work was supported by the Deanship of Scientific Research, Vice Presidency for Graduate Studies and Scientific Research, King Faisal University, Saudi Arabia [Grant No. KFU254684].

Conflict of interest

All authors declare no conflicts of interest in this paper.

References

1. A. E. Hamza, K. S. Mohamed, A. Mustafa, K. Aldwoah, M. Hassan, H. Saber, Abundant novel stochastic fractional solitary wave solutions of a new extended (3+1)-dimensional Kadomtsev-Petviashvili equation, *Alex. Eng. J.*, **119** (2025), 45–55. https://doi.org/10.1016/j.aej.2025.01.073
2. R. Roy, H. K. Barman, M. A. Akbar, J. F. Gómez-Aguilar, Bright-dark solitary wave solutions to the nonlinear fractional Boussinesq and breaking soliton equations, *Nonlinear Dyn.*, **113** (2025), 8819–8837. https://doi.org/10.1007/s11071-024-10516-y
3. Z. Shi, J. Zhou, D. Song, J. Cui, M. Yuan, C. Miao, The viscoelastic stress wave propagation model based on fractional derivative constitutive, *Int. J. Impact Eng.*, **202** (2025), 105330. https://doi.org/10.1016/j.ijimpeng.2025.105330
4. W. W. Mohammed, M. M. Khatun, M. S. Algolam, R. Sidaoui, M. A. Akbar, Analytical solitary wave solutions of fractional Tzitzeica equation using expansion approach: Theoretical insights and applications, *Fractal Fract.*, **9** (2025), 438. https://doi.org/10.3390/fractalfract9070438
5. M. A. I. Essawy, R. A. Rezk, A. M. Mostafa, Fractional dynamics of laser-induced heat transfer in metallic thin films: Analytical approach, *Fractal Fract.*, **9** (2025), 373. https://doi.org/10.3390/fractalfract9060373
6. U. Younas, J. Muhammad, M. A. S. Murad, D. K. Almutairi, A. Khan, T. Abdeljawad, Investigating the truncated fractional telegraph equation in engineering: Solitary wave solutions, chaotic and sensitivity analysis, *Results Eng.*, **25** (2025), 104489. https://doi.org/10.1016/j.rineng.2025.104489
7. M. Al-Amin, M. N. Islam, M. A. Akbar, Computational analysis and wave propagation behavior of hyper-geometric soliton waves in plasma physics via the auxiliary equation method, *Partial Differ. Equ. Appl. Math.*, **14** (2025), 101231. https://doi.org/10.1016/j.padiff.2025.101231
8. H. Ma, R. U. Rahman, S. Manukure, Dynamical analysis and bifurcations in a fractional integrable equation, *Alex. Eng. J.*, **125** (2025), 600–623. https://doi.org/10.1016/j.aej.2025.03.138
9. D. Chou, S. M. Boulaaras, H. U. Rehman, I. Iqbal, K. Khushi, Fractional nonlinear doubly dispersive equations: Insights into wave propagation and chaotic behavior, *Alex. Eng. J.*, **114** (2025), 507–525. https://doi.org/10.1016/j.aej.2024.11.097
10. A. Khan, M. I. Liaqat, M. Younis, A. Alam, Approximate and exact solutions to fractional order Cauchy reaction-diffusion equations by new combine techniques, *J. Math.*, **2021** (2021), 5337255. https://doi.org/10.1155/2021/5337255
11. E. M. Özkan, A. Özkan, On exact solutions of some important nonlinear conformable time-fractional differential equations, *SeMA J.*, **80** (2023), 303–318. https://doi.org/10.1007/s40324-022-00290-5
12. A. Özkan, E. M. Özkan, O. Yildirim, On exact solutions of some space-time fractional differential equations with M-truncated derivative, *Fractal Fract.*, **7** (2023), 255. https://doi.org/10.3390/fractalfract7030255
13. R. U. Rahman, A. F. Al-Maaitah, M. Qousini, E. A. Az-Zo'bi, S. M. Eldin, M. Abuzar, New soliton solutions and modulation instability analysis of fractional Huxley equation, *Results Phys.*, **44** (2023), 106163. https://doi.org/10.1016/j.rinp.2022.106163

14. Z. Odibat, S. Momani, The variational iteration method: An efficient scheme for handling fractional partial differential equations in fluid mechanics, *Comput. Math. Appl.*, **58** (2009), 2199–2208. https://doi.org/10.1016/j.camwa.2009.03.009

15. O. Guner, A. Bekir, H. Bilgil, A note on exp-function method combined with complex transform method applied to fractional differential equations, *Adv. Nonlinear Anal.*, **4** (2015), 201–218. https://doi.org/10.1515/anona-2015-0019

16. B. Lu, The first integral method for some time fractional differential equations, *J. Math. Anal. Appl.*, **395** (2012), 684–693. https://doi.org/10.1016/j.jmaa.2012.05.066

17. H. Jafari, N. Kadkhoda, A. Biswas, The G'/G-expansion method for solutions of evolution equations from isothermal magnetostatic atmospheres, *J. King Saud Univ. Sci.*, **25** (2013), 57–62. https://doi.org/10.1016/j.jksus.2012.02.002

18. N. Kadkhoda, H. Jafari, Analytical solutions of the Gerdjikov-Ivanov equation by using $\exp(-\phi(\xi))$ -expansion method, *Optik*, **139** (2017), 72–76. https://doi.org/10.1016/j.ijleo.2017.03.078

19. H. Jafari, H. Tajadodi, D. Baleanu, A. A. Al-Zahrani, Y. A. Alhamed, A. H. Zahid, Exact solutions of Boussinesq and KdV-mKdV equations by fractional sub-equation method, *Rom. Rep. Phys.*, **65** (2013), 1119–1124.

20. A. C. Cevikel, A. Bekir, E. H. M. Zahran, Novel exact and solitary solutions of conformable Huxley equation with three effective methods, *J. Ocean Eng. Sci.*, 2022. In Press. https://doi.org/10.1016/j.joes.2022.06.010

21. T. El-Sayed El-Danaf, M. A. Zaki, W. Moenaaem, New numerical technique for solving the fractional Huxley equation, *Int. J. Numer. Method. H.*, **24** (2014), 1736–1754. https://doi.org/10.1108/HFF-07-2013-0216

22. M. Inc, M. Partohaghighi, M. A. Akinlar, P. Agarwal, Y. M. Chu, New solutions of fractional-order Burger-Huxley equation, *Results Phys.*, **18** (2020), 103290. https://doi.org/10.1016/j.rinp.2020.103290

23. J. Shi, X. Yang, X. Liu, A novel fractional physics-informed neural networks method for solving the time-fractional Huxley equation, *Neural Comput. Appl.*, **36** (2024), 19097–19119. https://doi.org/10.1007/s00521-024-10177-3

24. A. S. V. R. Kanth, K. Aruna, K. Raghavendar, Natural transform decomposition method for the numerical treatment of the time fractional Burgers-Huxley equation, *Numer. Meth. Part. Differ. Equ.*, **39** (2023), 2690–2718. https://doi.org/10.1002/num.22983

25. R. Wang, Y. Chen, L. Qiao, J. Huang, Numerical methods for studying neuronal dynamics in the stochastic fractional Hodgkin-Huxley model, *Phys. Lett. A*, **561** (2025), 130966. https://doi.org/10.1016/j.physleta.2025.130966

26. A. Majeed, M. Kamran, N. Asghar, D. Baleanu, Numerical approximation of inhomogeneous time fractional Burgers-Huxley equation with B-spline functions and Caputo derivative, *Eng. Comput.*, **38** (2022), 885–900. https://doi.org/10.1007/s00366-020-01261-y

27. S. H. Weinberg, Membrane capacitive memory alters spiking in neurons described by the fractional-order Hodgkin-Huxley model, *PloS One*, **10** (2015), e0126629. https://doi.org/10.1371/journal.pone.0126629

28. N. Kadkhoda, H. Jafari, Application of fractional sub-equation method to the space-time fractional differential equations, *Int. J. Adv. Appl. Math. Mech.*, **4** (2017), 1–6.

29. S. E. Tutam, M. Akar, Exact solutions of the generalized Huxley-Burgers' equations, *Mod. Phys. Lett. B*, **39** (2025), 2450452. https://doi.org/10.1142/S0217984924504529

30. Z. Rahman, M. Z. Ali, H. O. Roshid, Closed form soliton solutions of three nonlinear fractional models through proposed improved Kudryashov method, *Chinese Phys. B*, **30** (2021), 050202. https://doi.org/10.1088/1674-1056/abd165

31. M. Kleczka, W. Kleczka, E. Kreuzer, Bifurcation analysis: A combined numerical and analytical approach, In: *Continuation and bifurcations: Numerical techniques and applications*, Dordrecht: Springer, 1990, 123–137. https://doi.org/10.1007/978-94-009-0659-4_8

32. S. T. R. Rizvi, S. O. Abbas, S. Ghafoor, A. Althobaiti, A. R. Seadawy, Soliton solutions with generalized Kudryashov method and study of variational integrators with Lagrangian to shallow water wave equation, *Mod. Phys. Lett. A*, **40** (2025), 2550043. https://doi.org/10.1142/S0217732325500439

33. M. Cai, C. Li, C. Wang, J. Shi, Effects of additive noise and variable coefficients on the exact solutions of the stochastic Kawahara equation, *Phys. Lett. A*, **554** (2025), 130723. https://doi.org/10.1016/j.physleta.2025.130723

34. A. Atangana, R. T. Alqahtani, Modelling the spread of river blindness disease via the Caputo fractional derivative and the beta-derivative, *Entropy*, **18** (2016), 40. https://doi.org/10.3390/e18020040

35. A. K. Shukla, J. C. Prajapati, On a generalization of Mittag-Leffler function and its properties, *J. Math. Anal. Appl.*, **336** (2007), 797–811. https://doi.org/10.1016/j.jmaa.2007.03.018

36. S. Akcagi, T. Aydemir, Comparison between the (G'/G)-expansion method and the modified extended tanh method, *Open Phys.*, **14** (2016), 88–94. https://doi.org/10.1515/phys-2016-0006

37. Y. Alhojilan, H. M. Ahmed, Novel analytical solutions of stochastic Ginzburg-Landau equation driven by Wiener process via the improved modified extended tanh function method, *Alex. Eng. J.*, **72** (2023), 269–274. https://doi.org/10.1016/j.aej.2023.04.005

38. A. Filiz, M. Ekici, A. Sonmezoglu, F-Expansion method and new exact solutions of the Schrödinger-KdV equation, *Sci. World J.*, **2014** (2014), 534063. https://doi.org/10.1155/2014/534063

39. S. S. Mahmood, M. A. Murad, S. S. Omer, S. S. Omer, S. J. Saeed, Traveling wave solutions of nonlinear evolution equations via the F-expansion method, *Comput. Method. Differ. Equ.*, 2025, 1-27. https://doi.org/10.22034/cmde.2025.66357.3092

40. C. Li, F. Zeng, Finite difference methods for fractional differential equations, *Int. J. Bifurcat. Chaos*, **22** (2012), 1230014. https://doi.org/10.1142/S02181274123001

41. R. U. Rahman, Z. Hammouch, A. S. A. Alsubaie, K. H. Mahmoud, A. Alshehri, E. A. Az-Zo'bi, et al., Dynamical behavior of fractional nonlinear dispersive equation in Murnaghan's rod materials, *Results Phys.*, **56** (2024), 107207. https://doi.org/10.1016/j.rinp.2023.107207

42. S. M. Y. Arafat, M. A. Saklayen, S. M. R. Islam, Analyzing diverse soliton wave profiles and bifurcation analysis of the (3+1)-dimensional mKdV-ZK model via two analytical schemes, *AIP Adv.*, **15** (2025), 015219. https://doi.org/10.1063/5.0248376

43. T. Han, K. Zhang, Y. Jiang, H. Rezazadeh, Chaotic pattern and solitary solutions for the (2+1)-dimensional beta-fractional double-chain DNA system, *Fractal Fract.*, **8** (2024), 415. https://doi.org/10.3390/fractalfract8070415

AIMS Press